Journal of Catalysis 282 (2011) 165–174

Contents lists available at ScienceDirect

Journal of Catalysis

journal homepage: www.elsevier.com/locate/jcat

Novel Pt/Mg(In)(Al)O catalysts for ethane and propane dehydrogenation

Pingping Sun [a], Georges Siddiqi [a], William C. Vining [a], Miaofang Chi [b], Alexis T. Bell [a,*]

[a] Department of Chemical and Bimolecular Engineering, University of California, Berkeley, CA 94720-1462, United States
[b] Oak Ridge National Laboratory, Oak Ridge, TN 37831-6064, United States

ARTICLE INFO

Article history:
Received 23 March 2011
Revised 5 June 2011
Accepted 7 June 2011
Available online 20 July 2011

Keywords:
Pt bimetallic catalyst
Mg(In)(Al)O
STEM
XAFS
Dehydrogenation

ABSTRACT

Catalysts for the dehydrogenation of light alkanes were prepared by dispersing Pt on the surface of a calcined hydrotalcite-like support containing indium, Mg(In)(Al)O. Upon reduction in H_2 at temperatures above 673 K, bimetallic particles of PtIn are observed by TEM, which have an average diameter of 1 nm. Analysis of Pt L_{III}-edge extended X-ray absorption fine structure (EXAFS) data shows that the In content of the bimetallic particles increases with increasing bulk In/Pt ratio and reduction temperature. Pt L_{III}-edge X-ray absorption near edge structure (XANES) indicates that an increasing donation of electronic charge from In to Pt occurs with increasing In content in the PtIn particles. The activity and selectivity of the Pt/Mg(In)(Al)O catalysts for ethane and propane dehydrogenation reactions are strongly dependent on the bulk In/Pt ratio. For both reactants, maximum activity was achieved for a bulk In/Pt ratio of 0.48, and at this In/Pt ratio, the selectivity to alkene was nearly 100%. Coke deposition was observed after catalyst use for either ethane or propane dehydrogenation, and it was observed that the alloying of Pt with In greatly reduced the amount of coke deposited. Characterization of the deposit by Raman spectroscopy indicates that the coke is present as highly disordered graphite particles <30 nm in diameter. While the amount of coke deposited during ethane and propane dehydrogenation are comparable, the effects on activity are dependent on reactant composition. Coke deposition had no effect on ethane dehydrogenation activity, but caused a loss in propane dehydrogenation activity. This difference is attributed to the greater ease with which coke produced on the surface of PtIn nanoparticles migrates to the support during ethane dehydrogenation versus propane dehydrogenation.

1. Introduction

Ethylene, propylene, and butene are used extensively to produce rubber, plastics and many other products. The conventional source of these light alkenes is steam cracking of alkanes, naphtha, or gas oil. This process is typically carried out at 1123 K and is not selective. For example, steam cracking of naphtha produces ethene yields of 30% and propene yields of 20%, with substantial quantities of methane and coke as byproducts. Catalytic dehydrogenation of alkanes provides an alternative for producing light alkenes as well as hydrogen, a product required for many refinery operations, most notably heteroatom removal. While thermal dehydrogenation, like steam cracking, is an endothermic process, it occurs at lower temperatures, 973–1073 K, but can also produce methane and coke as byproducts.

Platinum is the most effective transition metal for promoting alkane dehydrogenation; however, in order to achieve high alkene selectivity, it must be promoted with an element, such as Sn, Zn, Ge, Ga, or In, which interacts with the Pt to form a bimetallic alloy [1–9]. Bimetallic nanoparticles of Pt and the alloying element have also been found to produce less coke [10–14], a product that can contribute to deactivation of the catalyst. Catalyst stability is further enhanced by using a metal oxide support free of acid sites that can promote carbon deposition through polymerization of the product alkene [14–19]. Recent work has shown that calcined hydrotalcite-like materials, referred to as Mg(Al)O, are ideal for this purpose [11,20,21]. Moreover, the Al cations present at the support surface help stabilize the dispersed metal particles against sintering [22].

Of the promoting elements listed earlier, the greatest attention has been given to Sn [13,14,23–29]. This element can be introduced by coimpregnation of Pt and Sn precursors into a metal oxide support or by first forming a supported Pt catalyst and then impregnating it with a solution containing the Sn precursor. The properties of the catalyst have been found to depend on the composition of the Pt and Sn precursors and the catalyst preparation procedure [14]. By contrast, the performance of PtIn catalysts is less dependent on the composition of the Pt and In precursors and the procedure used for catalyst preparation [30]. PtIn catalysts have also been found to be more homogenous in composition than PtSn particles [31] and to be stable for dehydrogenation of C_4 and C_5 alkanes [3]. Consequently, PtIn catalysts could potentially be effective catalysts for dehydrogenation of light alkanes in general.

* Corresponding author. Fax: +1 510 642 4778.
E-mail address: alexbell@uclink.berkeley.edu (A.T. Bell).

0021-9517/$ - see front matter © 2011 Elsevier Inc. All rights reserved.
doi:10.1016/j.jcat.2011.06.008

We have recently reported a novel approach for producing PtGa bimetallic nanoparticles exhibiting high activity and selectivity for ethane and propane dehydrogenation, as well as reduced carbon deposition [32]. These catalysts were prepared by dispersing Pt nanoparticles onto a calcined hydrotalcite-like support containing Ga, Mg(Ga)(Al)O. Upon H_2 reduction of Pt/Mg(Ga)(Al)O at 873 K, a part of the Ga^{3+} cations at the surface of the support were reduced and the resulting Ga atoms formed PtGa bimetallic particles by alloying with the supported Pt particles. Since In can be introduced into the support in a manner similar to Ga, we undertook an investigation of the properties of Pt/Mg(In)(Al)O catalysts for light alkane dehydrogenation. Here we report on the preparation, characterization, and evaluation of such catalysts for ethane and propane dehydrogenation. XANES and EXAFS were used to track the alloy composition of the catalyst as a function of the bulk In/Pt ratio and examine the effect of reduction temperature on alloy formation. Information about metal particle size before and after catalyst use was obtained by STEM, whereas Raman spectroscopy was used to identify type of coke deposited following ethane or propane dehydrogenation.

2. Experimental

2.1. Catalyst preparation

Mg(In)(Al)O was synthesized using the following procedure. A mass of 58.31 g of $Mg(NO_3)_2\,6H_2O$ (Alfa Aesar, 98–102%), appropriate amounts (depending on the desired In loading) of $Al(NO_3)_3{\cdot}9H_2O$ (Alfa Aesar, 98–102%) and $In(NO_3)_3{\cdot}\times H_2O$ (Alfa Aesar, 99.9%) were dissolved in 250 ml deionized water, and 1.2 g of Na_2CO_3 (EMD Chemicals Inc, 99.5%) and 11 g of NaOH (Fisher Scientific, 98.3%) were dissolved in 250 ml deionized water. These two solutions were then mixed dropwise with stirring, at about 333 K in about 20 min, and aged at room temperature for 18 h. The resulting suspension was filtered, and the solid product dried in air overnight at 383 K. The hydrotalcites-like material obtained in this manner was heated in air to 973 K at 2 K/min and maintained at this temperature for 10 h to obtain the calcined support, Mg(In)(Al)O. Mg(Al)O was prepared in a similar manner.

The same amount of Pt was dispersed onto 1 g of the calcined support by incipient wetness impregnation, using a solution containing 21 mg of Pt(acetylacetonate)$_2$ (Sigma Aldrich, 99.99%) dissolved in 1.5 ml toluene. The resulting mixture was stirred until powdery, then left at room temperature in air for 2 h, and finally dried overnight at 383 K in an oven. After drying, the catalyst was reduced at 723 K for 2 h (5 K/min temperature ramp) in 10% H_2/Ar (60 cm^3/min). In this manner, a series of Pt/Mg(In)(Al)O catalysts were prepared with different bulk In/Pt ratio.

2.2. Catalyst characterization

The content of Pt, Mg, Al and In were determined by Galbraith Laboratories (Knoxville, TN) using inductively coupled plasma optical emission spectroscopy. The BET surface area of Pt/Mg(Al)(In)O was determined by the multi-point method using an Autosorb-1 instrument (Quantachrome Corporation). Prior to measuring the adsorption isotherm, each sample was degassed at 573 K for 22–24 h. The hydrotalcite-like material was characterized by X-ray powder diffraction before and after calcination, using a Siemens Diffractometer D 5000 with CuKα radiation ($\lambda = 1.5418$ Å) at 20 kV and 5 mA. The samples were scanned from 2θ values of 5° to 70° with a step size of 0.02° and a dwell time of 1.0 s. The dispersion of Pt on Pt/Mg(Al)(In)O was determined by H_2 chemisorption using a AutoChem II 2920 (Micromeritics Instrument Corporation). About 60 mg of Pt/Mg(In)(Al)O was loaded into a quartz cell and then reduced in flowing 10% H_2/Ar (50 cm^3/min). The temperature of the sample was raised at 5 K/min to 873 K and then maintained at this level for 2 h. The sample was then flushed in flowing Ar for 90 min and then cooled down to 313 K. The uptake of chemisorbed hydrogen was then measured by determining the uptake of H_2 from pulses using a TCD detector. The pulse size was 50 cm^3/g, and the time between pulses was 10 min.

Electron micrographs of the support, with and without Pt, were taken using an aberration-corrected FEI Titan 80/300-kV TEM/STEM located at Oak Ridge National Laboratory. Bright-field and high angle annular dark-field (HAADF) STEM images were recorded simultaneously to get full information of the microstructure. HAADF images were acquired with a 300-kV accelerating voltage with a convergence angle of 30 mrad and a large inner collection angle of 75 mrad. The contrast of the acquired HAADF images is sensitive to atomic number. To minimize electron beam radiation on the sample, all images were acquired in regions that had not been previously illuminated, shortly after the electron beam had been aligned in a neighboring region. Electron energy loss spectra were acquired for 3 s with a convergence angle of 30 mrad and collection angle of 35 mrad. The data were processed through DigitalMicrograph.

Pt L_{III}- and In K-edge XAS data were collected at the Advanced Photon Source at Argonne National Lab on beamline 10-BM with a Si(1 1 1) monochromator crystal detuned by 40%. The sample was located between two ionization chambers, and a reference foil was placed after the second ionization chamber for energy calibration. Nitrogen and argon gas was used in the ionization chambers for Pt L_{III}- and In K-edges, respectively, and all samples were investigated in transmission mode. All six samples with In/Pt ratios (In/Pt = 0, 0.33, 0.48, 0.88, 1.7, 5.6) were prepared simultaneously under three different pretreatment conditions: 723 K for 1 h in 4% H_2/He at 100 cm^3/min, 873 K for 1 h in 4% H_2/He at 100 cm^3/min, and 873 K for 1 h in 10% O_2/N_2 after pretreatment at 873 K in hydrogen. All samples were cooled to ambient temperature in He flowing at 100 cm^3/min and then transferred to the beamline for immediate EXAFS characterization.

EXAFS data were analyzed using the program Ifeffit and the graphical user interfaces Athena and Artemis [33]. The incident photon energy was calibrated to a reference Pt foil. The edge energy was set to the first inflection point on the rising part of the absorbance edge. Data were normalized using a pre-edge line fit from −150 to −50 eV below the edge and a quadratic polynomial with a k-weight of two from 150 to 749 eV above the edge energy. A spline was fit to the data $0 < k < 15$ Å^{-1} after the edge. The data for $3.5 < k < 12.1$ Å^{-1} were fit from 1.8 to 3.2 Å for catalysts treated in hydrogen at 873 K and from 1.4 to 3.2 Å for the other two pretreatments using k-weights of 1, 2, and 3. For all pretreatments, the initial Pt and In paths were taken to be 2.8 Å. The same mean square disorder, σ^2, and edge energy were used for both paths, but the path lengths were allowed to vary independently. For the samples pretreated in hydrogen at 723 K, a third oxygen path was added at a distance of 2 Å, and the bond length and coordination number were allowed to vary separately. The same structural disorder parameter and edge energy for the Pt and In paths were used in the oxygen path. Theoretical standards were constructed using known crystal structures of PtIn alloys [34], as well as Pt oxides [34].

2.3. Catalyst testing

Reactions were carried out in a quartz reactor with an inner diameter of 7 mm. Prior to testing, the catalyst (0.025 g, 0.25–0.5 mm particle size) was heated at 10 K/min to 873 K in 20% H_2 in He and then maintained at this temperature for 1 h. The catalyst bed was heated by a three-zone furnace (Applied Test System, Inc.)

controlled by Watlow 988 controllers. The temperature of the catalyst bed was measured by two thermocouples centered axially inside the reactor, one at the top and one at the bottom of the catalyst bed. Brooks Mass Flow Controllers (MFC) were used to deliver the flow of each gas. Measurements of catalyst activity and selectivity were carried out at 873 K, using 0.025 g of catalyst and a feed consisting of 20% ethane or propane, 25% hydrogen, and the balance He flowing at 60 cm^3/min [32]. All experiments were performed in the kinetic regime. Internal mass transport limitations were not observed as evidenced by a linear Arrhenius plot and satisfaction of the Weisz–Prater criterion [35].

2.4. Coke measurement

Coke deposition occurred during the exposure of the catalyst to ethane or propane. The amount of coke deposited was determined by combustion of the deposited material. Prior to combustion, the catalyst (0.025 g) was purged with flowing He (60 cm^3/min) at 873 K for 5 min, and then exposed it to a mixture of 5% O_2 in He flowing at 60 cm^3/min. The CO_2 generated were monitored by online mass spectrometry (MS). The amount of deposited coke was calculated from the amount of generated CO_2. Regeneration of the catalysts was done by oxidizing the catalyst in a flow of 10% O_2 in He (100 cm^3/min) for 20 min and then reducing the catalyst in a flow of 20% H_2 in He (100 cm^3/min) for 30 min. Prior to changing the gas composition, the reactor was flushed with helium.

The Raman spectra of coke deposited during alkane dehydrogenation were performed with an epi-illumination, confocal Raman microscope (LabRam HR, Horiba Jobin Yvon). A diode-pumped solid-state 532-nm laser (Torus, Laser Quantum) was used as the excitation source. The back-scattered light was filtered by a 532-nm edge filter and channeled into a spectrograph/charge-coupled device detector (Andor). The laser power was 3–9 mw, and the resolution of the apparatus was 1 cm^{-1}. The data acquisition time was between 4 and 15 s, and 8–20 scans were acquired depending on the strength of the carbon signal.

3. Results and discussion

3.1. Catalyst characterization before reaction

A list of all samples studied is presented in Table 1. The Mg/(Al + In) ratio was maintained close to 5 for the majority of the samples, and the In/Al ratio was varied from 0 to 0.167. The Pt content was maintained between 0.7 wt.% and 0.8 wt.%, whereas the In/Pt ratio varied from 0 to 10.7.

Fig. 1 shows the XRD pattern of the dried, as-synthesized support (top) and the same material after calcination (bottom). Prior to calcination, the XRD pattern is characteristic of the layered double hydroxide structure of hydrotalcite [36]. After calcination at 973 K, the structure of the solid changes from orthorhombic to cubic, corresponding to the transformation of a two-dimensional layered structure to a three-dimensional structure, analogous to periclase MgO. The broad peaks of both materials are indicative of small crystalline particles or a partially amorphous phase. Similar changes in the XRD patterns were observed for all support materials, independent of the In/Al ratio.

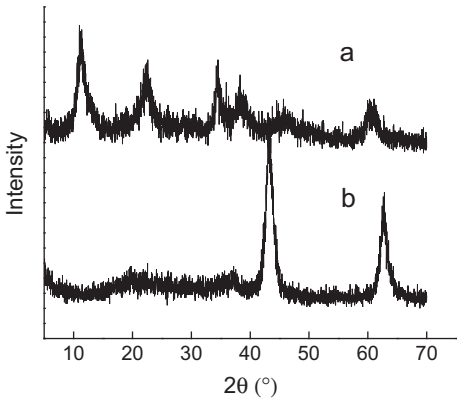

Fig. 1. XRD of as-synthesized (a) and calcined hydrotalcites (b).

Table 2 lists the surface areas of the calcined mixed oxide materials. Mg(Al)O has a surface area of 176 m^2/g and a pore volume of 0.6 cm^3/g. Neither the surface area nor pore volume of Mg(In)(Al)O changed much upon increasing the In content from 0–5.1 wt.%. Minimal change in the surface area and pore volume occurred upon the dispersion of Pt onto the support. The ratio of H atoms adsorbed to the total number of Pt atoms in the catalyst is also presented in Table 2. For Pt/Mg(Al)O, this ratio is 0.84, which means that the dispersion of the Pt is 84%. As discussed in the next paragraph, the Pt particle size estimated from the dispersion, 1.3 nm, is consistent with that determined from STEM images, about 1 nm, independent of the bulk In/Pt ratio. The ratio of adsorbed H atoms to total Pt atoms measured for the Pt/Mg(Al)(In)O samples is a function of the In/Pt ratio. This ratio is 0.94 when In/Pt = 0.48 and decreases rapidly with increasing In/Pt ratio, reaching a value of 0.06 when In/Pt = 10.7. Since, as discussed later, the size of the PtIn particles remains essentially the same with increasing bulk In/Pt ratio, the observed decrease in H/Pt ratio is ascribed to increase coverage of the metal nanoparticles by In. This interpretation is consistent with previous research, showing that the adsorption of H_2 on Pt alloyed with Sn and Ga is reduced by the presence of the alloying metal on the particle surface because the alloying metal does not adsorb H_2 [37,38].

A STEM image of Pt/Mg(In)(Al)O-0.88 is shown in Fig. 2. After calcination, the support still exhibits a partially layered structure, similar to that seen earlier for calcined Mg(Al)O [39]. Small metallic particles about 1 nm in diameter are observed distributed evenly over the support. Similar particle size distributions were observed for all catalysts with In/Pt ratio from 0 to 10.7, suggesting that the presence of In in the support does not change the size of the metal particles relative to that observed in the absence of In.

Table 1
Composition of all catalysts.

Sample name[a]	Pt wt.%	In wt.%	Starting ratio Mg:Al:In	Mg/(Al + In)	In/Al	In/Pt
Pt/Mg(Al)O	0.70	0	100:10:0	5.09	0	–
Pt/Mg(Al)(In)O-0.33	0.89	0.171	100: 9.95:0.05	5.13	0.0047	0.33
Pt/Mg(Al)(In)O-0.48	0.71	0.201	100: 9.9: 0.10	4.82	0.0065	0.48
Pt/Mg(Al)(In)O-0.88	0.83	0.428	100: 9.86: 0.14	4.90	0.010	0.88
Pt/Mg(Al)(In)O-1.7	0.67	0.674	100: 9.75: 0.25	4.60	0.021	1.7
Pt/Mg(Al)(In)O-5.6	0.76	2.49	100: 9: 1	5.31	0.083	5.6
Pt/Mg(Al)(In)O-10.7	0.81	5.12	100: 8: 2	5.02	0.167	10.7

[a] The letter refers to support name, the number afterward refers to In/Pt ratio of the catalyst.

Table 2
Catalyst surface area (BET), pore volume, average pore radius and percent of exposed Pt sites.

Sample name	Exposed Pt sites (%)	Surface area (m^2/g)	Pore volume (cm^3/g)	Average pore radius (Å)
Pt/Mg(Al)O	84	176	0.60	70.0
Pt/Mg(Al)(In)O-0.33	84	148	0.55	73.7
Pt/Mg(Al)(In)O-0.48	94	161	0.61	75.9
Pt/Mg(Al)(In)O-0.88	65	167	0.75	89.8
Pt/Mg(Al)(In)O-1.7	35	191	0.58	60.3
Pt/Mg(Al)(In)O-5.6	12	158	0.49	62.1
Pt/Mg(Al)(In)O-10.7	6	161	0.61	75.9

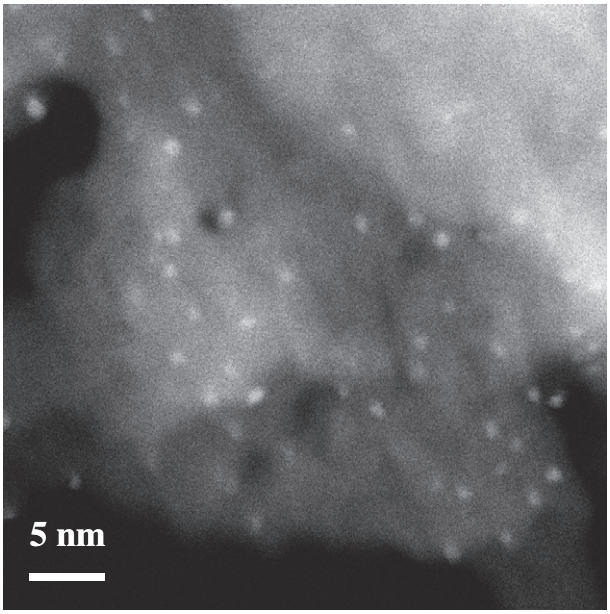

Fig. 2. STEM of Pt/Mg(In)(Al)O 0.88 before reaction.

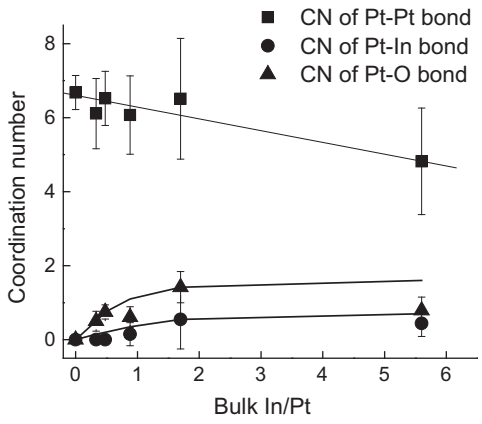

Fig. 3. Pt–Pt, Pt–In, Pt–O coordination numbers determined from Pt L_{III} edge. All EXAFS data were acquired after reduction with 100 cm^3/min of 4% H_2/He at 723 K for 1 h. Samples were cooled to ambient temperature in 100 cm^3/min of He flow before acquiring data. The error bars are the error in the coordination number determined by the best fit for each sample.

EXAFS spectra of Pt/Mg(Al)O and Pt/Mg(In)(Al) reduced in H_2 at 723 K (see supplementary material) were analyzed to determine the coordination numbers for Pt–Pt, Pt–In, and Pt–O nearest neighbors. The results are presented in Table 3 and Fig. 3 for catalysts prepared with bulk In/Pt ratio between 0 and 5.6. The data show that with increasing In/Pt ratios, the Pt–Pt coordination number decreases monotonically from 6.7 to 4.8, as the Pt–In and Pt–O coordination numbers increase from 0 to about 0.5 and 1.4. The appearance of Pt–In nearest neighbors as the bulk In/Pt ratio increases indicates that catalyst reduction at 723 K is sufficient to enable some of the In^{3+} cations present at the support surface and proximate to the Pt particles to be reduced, and resulting In atoms to form PtIn alloys with the Pt particles. This interpretation is consistent with the observation that In_2O_3 undergoes reduction in H_2 above 673 K [40]. It is notable that in the absence of In, catalyst reduction at 723 K is sufficient to remove all oxygen. However, when In is present in the support, the Pt–O coordination number rises slightly. Since the metal nanoparticles are very small (~1 nm), it is quite possible that the O atoms are present predominantly on the surface of the particles, rather than in the bulk.

Pt L_{III} edge XANES data acquired after catalyst reduction at 723 K are shown in Fig. 4. All samples show similar edge energies, but the intensity of the white line is higher for samples with In present, than for the sample without In. This might be due to Pt–O bonding in the In containing samples, in contrast to In-free samples, leading to an increase d-orbital vacancy and, hence, an increase in the white line intensity. It has generally been observed that the formation Pt alloys, such as PtSn [41], PtCu [42], PtIn [30], PtAu [43], leads to a decrease in white line intensity of Pt L_{III} edge. The white line intensity does not show a systematic change with In/Pt bulk ratios, however, quite possibly because the white line intensity is affected by both In and O. The oxygen effect may dominate, since the white line intensity correlates with the Pt–O coordination number.

Table 4 and Fig. 5 show that following hydrogen reduction at 873 K, the Pt–O coordination number is zero independent of the bulk In/Pt ratio. However, as the bulk In/Pt ratio increases, the

Table 3
EXAFS fitting parameters for Pt/Mg(In)(Al)O after reaction in 4% H_2/He for 1 h at 723 K. The data ($3.5 < k < 12.1$ $Å^{-1}$) were fit ($1.4 < R < 3.2$ Å) with one Pt and one In backscattering path. The amplitude reduction factor, S_0^2, was fixed to a value of 1 during the fit.

Catalyst	ΔE_0 (eV)	σ^2 ($Å^2$)	CN_{Pt-In}	R_{Pt-O} (Å)	CN_{Pt-In}	R_{Pt-In} (Å)	CN_{Pt-Pt}	R_{Pt-Pt} (Å)	*R*-factor
Pt/Mg(Al)O	5.4 ± 0.7	0.007 ± 0.001	–	–	–	–	6.7 ± 0.5	2.73 ± 0.01	0.003
Pt/Mg(Al)(In)O-0.33	4.3 ± 1.6	0.009 ± 0.001	0.5 ± 0.27	1.94 ± 0.05	–	–	6.1 ± 1.0	2.72 ± 0.01	0.020
Pt/Mg(Al)(In)O-0.48	5.9 ± 1.1	0.008 ± 0.001	0.75 ± 0.19	1.95 ± 0.03	–	–	6.5 ± 0.7	2.74 ± 0.01	0.008
Pt/Mg(Al)(In)O-0.88	5.0 ± 2.4	0.008 ± 0.002	0.61 ± 0.28	1.95 ± 0.04	0.15 ± 0.31	2.68 ± 0.18	6.1 ± 1.1	2.74 ± 0.02	0.007
Pt/Mg(Al)(In)O-1.7	7.2 ± 3.6	0.011 ± 0.002	1.42 ± 0.42	1.99 ± 0.04	0.55 ± 0.80	2.86 ± 0.08	6.5 ± 1.6	2.74 ± 0.02	0.012
Pt/Mg(Al)(In)O-5.6	2.0 ± 3.4	0.010 ± 0.003	0.79 ± 0.36	1.92 ± 0.05	0.44 ± 0.35	2.65 ± 0.10	4.8 ± 1.4	2.71 ± 0.03	0.020

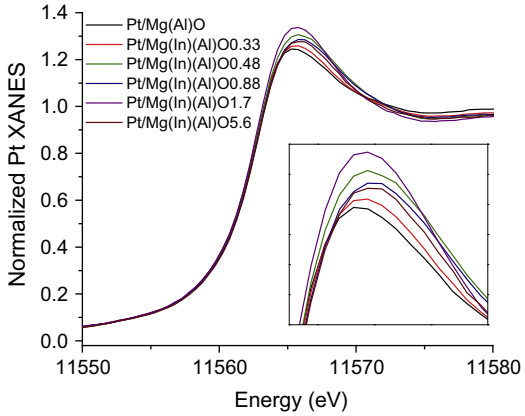

Fig. 4. Pt L_{III} XANES for Pt/Mg(Al)(In)O catalysts after treatment in 4% H_2/He for 1 h at 723 K. Samples were cooled to ambient temperature in He flow before data acquisition. The inset is an enlargement of the normalized edge height.

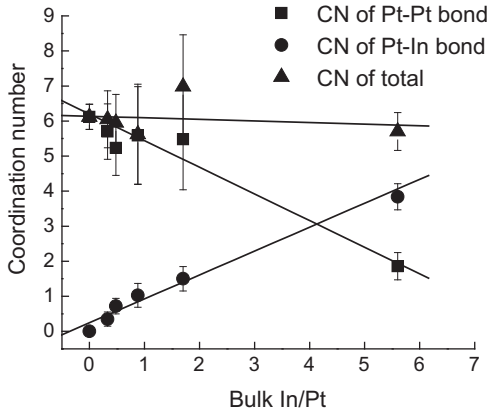

Fig. 5. Pt–Pt and Pt–In coordination numbers determined from Pt L_{III} edge. All EXAFS data were acquired after reduction with 100 cm^3/min of 4% H_2/He at 873 K for 1 h. Samples were cooled to ambient temperature in 100 cm^3/min of He flow before acquiring data. The error bars are the error in the coordination number and were determined by the best fit for each sample.

Pt–Pt coordination number decreases and the Pt–In coordination number increases. This trend indicates that the In content of the PtIn alloy particles formed upon reduction increases monotonically with increasing In/Pt ratio. Since the total coordination number (sum of CN_{PtPt} and CN_{PtIn}) is ~6 for In/Pt ratios 0–5.6, it is concluded that the diameters of the supported alloy particles do not change significantly with increasing In content, consistent with observations by STEM.

If it is assumed that In is uniformly distributed throughout the alloy, then the fraction of In contained in the supported PtIn nanoparticles can be estimated from the relationship $CN_{Pt-In}/(CN_{Pt-Pt} + CN_{Pt-In})$ assuming isostructural, spherical particles. The atomic fraction of In in the alloy particles calculated this way is listed in Table 5. It is apparent from these results that the fraction of the alloy consisting of In increases almost linearly with the bulk In/Pt ratio, in Fig. 7.

Tables 3 and 4 show that the Pt–Pt bond distance for Pt/Mg(Al)O reduced at both 723 K and 873 K is 2.73–2.74 Å, which is smaller than that for bulk Pt, 2.77 Å. The decrease in metallic bond distance with decreasing coordination is commonly observed [44]. This phenomenon is due to lattice relaxation of smaller particles (1–5 nm), which could result in 10% decrease in the Pt–Pt bond distance relative to that of bulk phase [45]. When In alloys with Pt, the Pt–Pt bond distance in the PtIn nanoparticles increases by no more than 0.03 Å. The calculated Pt–In bond distance exhibits more variation from sample to sample than the calculated Pt–Pt distance, but on average is 2.71 Å, which is comparable to the PtPt distance is consistent. The calculated Pt–In distance is consistent with those observed for PtIn alloys (2.73–2.95 Å) [34], but the accuracy with which this distance can be determined does not allow assignment to a particular PtIn alloy composition.

Fig. 6 shows Pt L_{III} XANES spectra for Pt/Mg(In)(Al)O catalysts reduced at 873 K. The intensity of the white line decreases slightly with increasing In amount but then increases at the highest In/Pt ratio. Pt L_{III} XANES characterizes dipole transitions from the $2p_{3/2}$ to the $5d_{5/2}$ orbital, since the $5d_{3/2}$ orbital is fully occupied [46,47]. Therefore, changes in the intensity of the white line indicate changes in the unoccupied states of the $5d_{5/2}$ orbital associated with metal oxidation and/or alloy formation. DFT calculations demonstrate that the white line density can also change with cluster size and cluster morphology because the density of states of nanometer-sized metal clusters is very different from that of the bulk phase [48,49]. This trend is consistent with experiments showing that the white line intensity for supported metal particles decreases with decreasing metal cluster size [44,50]. Since reduction at 873 K removes all oxygen from the supported nanoparticles and the size of the nanoparticles does not change with increasing bulk In/Pt ratio, the effects of Pt oxidation by O and changes in particle size with bulk In/Pt ratio on the intensity of the white line can be ruled out. As a result, the observed changes in the white line intensity of Pt L_{III} XANES spectra shown in Fig. 6 can only be attributed to the formation of a PtIn alloy.

It is also observed that following reduction at 873 K, there is an increase in the Pt L_{III} edge energy by about 1 eV with increasing bulk In/Pt ratio. This shift in edge is a further indicator of alloy formation. This trend is similar to that observed in XPS measurements

Table 5
Estimated PtIn alloy compositions.

Sample name	Bulk In/Pt	In/(Pt + In) alloy (%)	In in reduced state (%)
Pt/Mg(Al)(In)O-0.33	0.33	6	20
Pt/Mg(Al)(In)O-0.48	0.48	12	25
Pt/Mg(Al)(In)O-0.88	0.88	16	17
Pt/Mg(Al)(In)O-1.7	1.7	21	13
Pt/Mg(Al)(In)O-5.6	5.6	67	12

Table 4
EXAFS fitting parameters of Pt/Mg(In)(Al)O after treatment in 4% H_2/He for 1 h at 873 K. The data ($3.5 < k < 12.1$ Å^{-1}) were fit ($1.8 < R < 3.2$ Å) with one Pt and one In backscattering path. The amplitude reduction factor, $S_{0,}^2$, was fixed to a value of 1 during the fit.

Catalyst	ΔE_0 (eV)	σ^2 (Å^2)	CN_{Pt-In}	R_{Pt-In} (Å)	CN_{Pt-Pt}	R_{Pt-Pt} (Å)	*R*-factor
Pt/Mg(Al)O	6.4 ± 0.4	0.0065 ± 0.0004	–		6.1 ± 0.4	2.74 ± 0.01	0.002
Pt/Mg(Al)(In)O-0.33	3.3 ± 1.5	0.007 ± 0.001	0.4 ± 0.2	2.64 ± 0.05	5.7 ± 0.8	2.72 ± 0.01	0.005
Pt/Mg(Al)(In)O-0.48	3.2 ± 1.6	0.006 ± 0.001	0.7 ± 0.2	2.70 ± 0.03	5.2 ± 0.8	2.74 ± 0.01	0.004
Pt/Mg(Al)(In)O-0.88	1.6 ± 2.4	0.006 ± 0.002	1.0 ± 0.3	2.72 ± 0.04	5.6 ± 1.4	2.75 ± 0.02	0.011
Pt/Mg(Al)(In)O-1.7	1.5 ± 2.1	0.008 ± 0.002	1.5 ± 0.4	2.71 ± 0.03	5.5 ± 1.4	2.76 ± 0.02	0.013
Pt/Mg(Al)(In)O-5.6	1.2 ± 0.8	0.009 ± 0.001	3.8 ± 0.4	2.69 ± 0.01	1.9 ± 0.4	2.77 ± 0.02	0.003

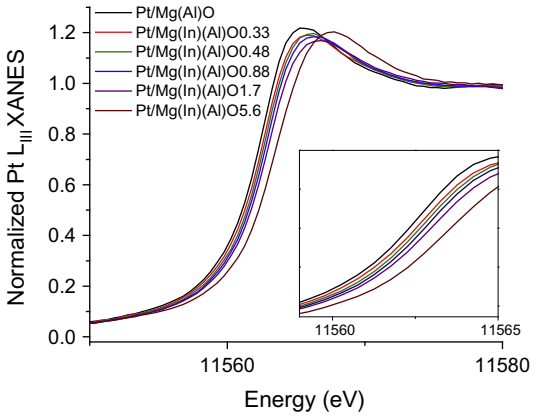

Fig. 6. Pt L_{III} XANES for Pt/Mg(Al)(In)O catalysts after treatment in 4% H_2/He for 1 h at 823 K. Samples were cooled to ambient temperature in He flow before data acquisition. Inset is close-up of edge shift.

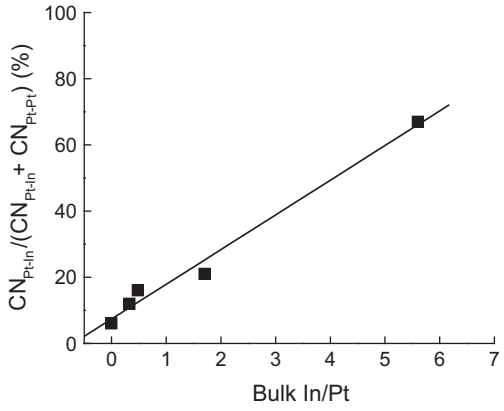

Fig. 7. Correlation between percent of alloy containing In with bulk In/Pt ratio.

when Pt is alloyed with Sn [25,51] or In [30]. The observed increase in Pt binding energy in both cases can be attributed to charge transfer from the alloying element to Pt since the electronegativity of Pt (2.28 eV) is higher than that of Sn (1.8 eV) or In (1.7 eV). Simulation of the XANES spectrum of PtAu nanoparticles further supports the assignment of shifts in the white line position to charge transfer occurring between the alloying elements [43].

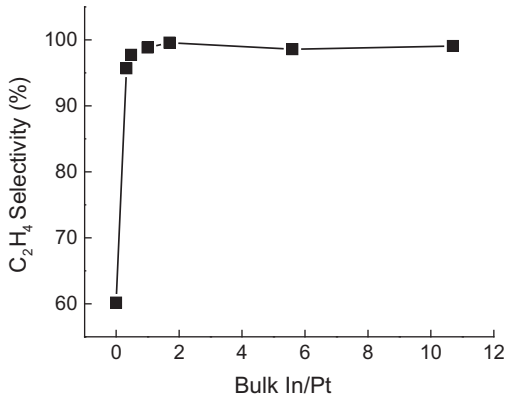

Fig. 9. Dependence of ethane selectivity on the bulk In/Pt ratio. Reaction conditions: *T*: 873 K, *m* = 25 mg, C_2H_6: 20%, total flow rate: 60 cm^3/min, H_2/C_2H_6 = 1.25).

3.2. Catalyst performance

The activity of Pt/Mg(In)(Al)O catalysts for ethane dehydrogenation is shown in Fig. 8 as a function of the bulk In/Pt ratio. The rate of C_2H_4 production per gram of catalyst (Fig. 8A) increases with In/Pt ratio for In/Pt = 0–0.48, and then decreases sharply as the In/Pt ratio is increased further. The turnover frequency for dehydrogenation was determined on the basis of the H_2 uptake measurements reported in Table 2. This definition of TOFs is based on the hypothesis that alkane dehydrogenation requires Pt sites and that only these sites will adsorb H atoms. Both assumptions have recently been confirmed by quantum chemical calculations conducted in our group. Fig. 8B shows that the TOF for ethane dehydrogenation increases by slightly more than a factor of two as the bulk In/Pt ratio increases from 0 to about 2 and then decreases monotonically for higher In/Pt ratios. Fig. 9 shows that the ethene selectivity increases rapidly with increasing In/Pt, reaching a value of nearly 100% for In/Pt > 0.33. It is noted that the only byproduct observed was methane. The amount of coke formation was recorded after two hours of reaction is shown in Fig. 10. As can be seen, the accumulation of coke decreases strongly with increased alloying of In with Pt. The highest accumulation of carbon was observed for Pt/Mg(Al)O. For this sample, the coke accumulated on the catalyst after 2 h of time on stream constituted only 0.3% of the total amount of the carbon contained in feed passed over the catalyst during this time. By contrast, typically 10% of the feed was converted to gaseous products (ethene,

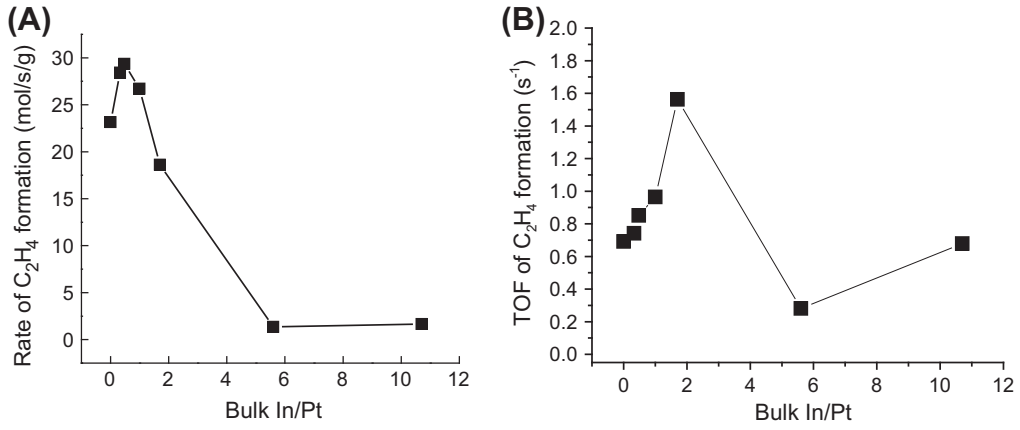

Fig. 8. In/Pt effect on C_2H_4 formation rate for C_2H_6 dehydrogenation when normalized by catalyst weight (A) and exposed Pt sites determined by H_2 chemisorption (B). Reaction conditions: *T*: 873 K, *m* = 25 mg, C_2H_6: 20%, total flow rate: 60 cm^3/min, H_2/C_2H_6 = 1.25).

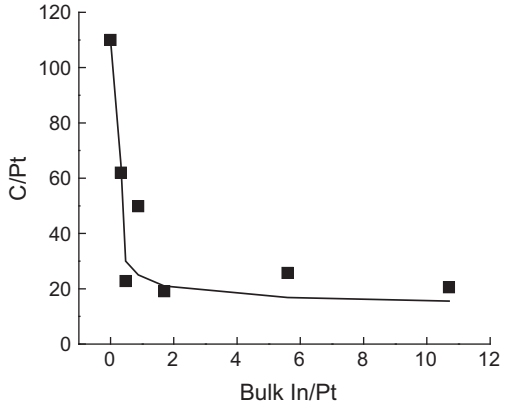

Fig. 10. Dependence of C/Pt ratio on bulk In/Pt ratio after 2 h time on stream of ethane dehydrogenation. Reaction conditions: *T*: 873 K, *m* = 25 mg, C_2H_6: 20%, total flow rate: 60 cm^3/min, H_2/C_2H_6 = 1.25).

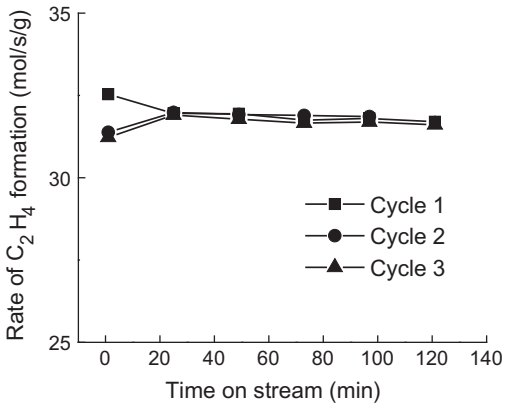

Fig. 11. Effects of catalyst cycling on rate of ethene formation versus time on stream. Reaction conditions: *T*: 873 K, *m* = 25 mg, C_2H_6: 20%, total flow rate: 60 cm^3/min, H_2/C_2H_6 = 1.25).

hydrogen, and methane); therefore, the selectivity to coke was 3% for Pt/Mg(Al)O, and even lower for the In-promoted catalysts.

The stability of the most active catalyst, Pt/Mg(In)(Al)O 0.48, was tested after coke had been removed from the catalyst by oxidation, and the catalyst was then reduced in H_2 at 873 K. As can be seen from Fig. 11, the catalyst is very stable with both time on stream and with repeated oxidation–reduction cycles.

Pt/Mg(In)(Al)O catalysts were also evaluated for propane dehydrogenation at 873 K. As seen in Fig. 12A, the rate of propane dehydrogenation passes through a maximum for a bulk In/Pt ratio of 0.48 and then rapidly declines to nearly zero. This behavior is similar to that observed for ethane dehydrogenation (see Fig. 8A), but the maximum rate for propane dehydrogenation is more than twofold higher than that for ethane dehydrogenation. Fig. 12B shows that in a manner similar to that observed for ethane dehydrogenation, the TOF for propane dehydrogenation passes through a maximum for In/Pt = 2. However, in contrast to what is seen for ethane dehydrogenation (see Fig. 9), the selectivity to propene rises rapidly to nearly 100% for a bulk In/Pt ratio of 0.48, passes through a maximum, and falls off for In/Pt ratios above about 2.0, shown in Fig. 13. As shown in the inset of this figure, the selectivities to CH_4, C_2H_6 and C_2H_4 increases from nearly zero when the In/Pt ratio is raised above 2.0. Fig. 14 shows that the amount of carbon accumulated on the catalyst after 2 h of time on stream decreases significantly as the bulk In/Pt ratio is increased from 0 to 0.48, and decreases further but more slowly as the In/Pt ratio is raised further.

The propane dehydrogenation activity of Pt/Mg(In)(Al)O 0.48 with time on stream is shown in Fig. 15. In contrast to what was seen for ethane dehydrogenation (see Fig. 13), the activity of this catalyst decreases significantly during the first 2 h of its use for propane dehydrogenation. On the other hand, as in the case of ethane dehydrogenation, removal of accumulated carbon after 2 h of time on stream and H_2 reduction at 873 K fully restores the original catalyst activity. Fig. 16 shows that the selectivity to propene rises slightly with time on stream to 99% and that this change of selectivity with time on stream is fully recovered each time the catalyst is cycled. The only products other than C_3H_6 and H_2 are CH_4, C_2H_6 and C_2H_4.

Catalysts used for ethane or propane dehydrogenation were examined by STEM and Raman spectroscopy with the goal of establishing whether metal particle sintering or carbon deposition was the cause of a loss in catalytic activity with time on stream. The average metal particle size after 2 h of reaction determined from STEM images of Pt/Mg(Al)O and Pt/Mg(In)(Al)O were very nearly the same as those determined prior to reaction, suggesting that particle sintering did not occur during alkane dehydrogenation.

Raman spectra of Pt/Mg(Al)O and Pt/Mg(In)(Al)O 0.88 taken after ethane and propane dehydrogenation, respectively, are presented in Figs. 17 and 18. The appearance of these spectra is virtually the same independent of which catalyst or alkane was used. Two broad bands are observed centered at 1332 cm^{-1} and 1585 cm^{-1}. These features are best assigned to the D and G bands,

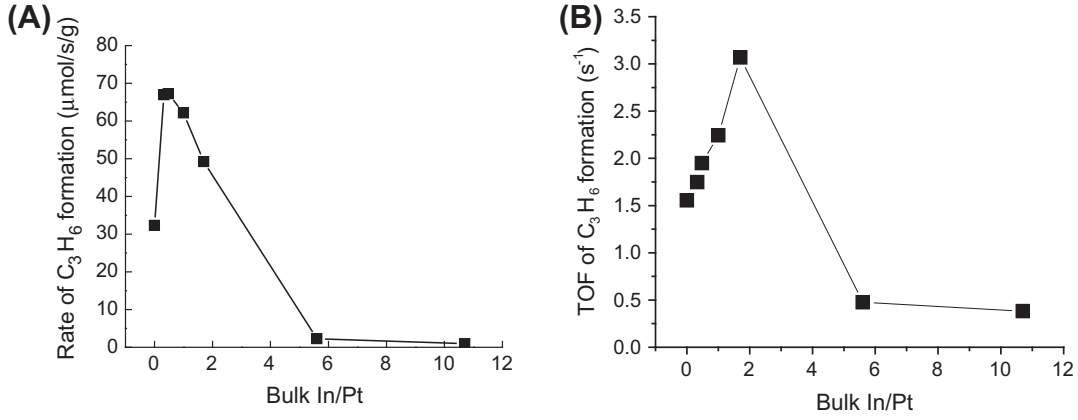

Fig. 12. In/Pt effect on C_3H_6 reaction rate for C_3H_8 dehydrogenation normalized by catalyst weight (A) and by exposed Pt sites determined by H_2 chemisorption (B). Reaction conditions: *T*: 873 K, *m* = 25 mg, C_3H_8: 20%, total flow rate: 60 cm^3/min, H_2/C_2H_6 = 1.25).

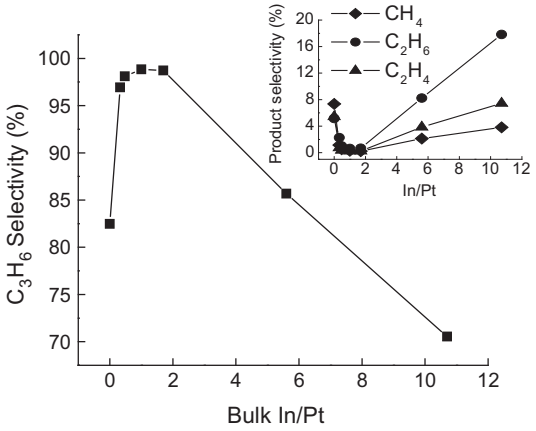

Fig. 13. Dependence of propene selectivity on bulk In/Pt ratio. The selectivities of CH_4, C_2H_6 and C_2H_4 are also listed in the inset figure. Reaction conditions: *T*: 873 K, *m* = 25 mg, C_3H_8: 20%, total flow rate: 60 cm^3/min, H_2/C_2H_6 = 1.25).

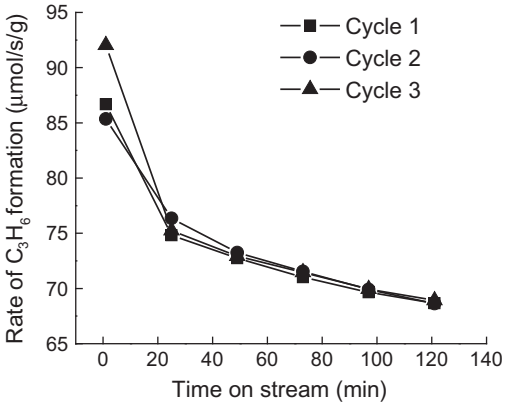

Fig. 15. Effects of catalyst cycling on rate of propene formation versus time on stream. Reaction conditions: *T*: 873 K, *m* = 25 mg, C_3H_8: 20%, total flow rate: 60 cm^3/min, H_2/C_2H_6 = 1.25).

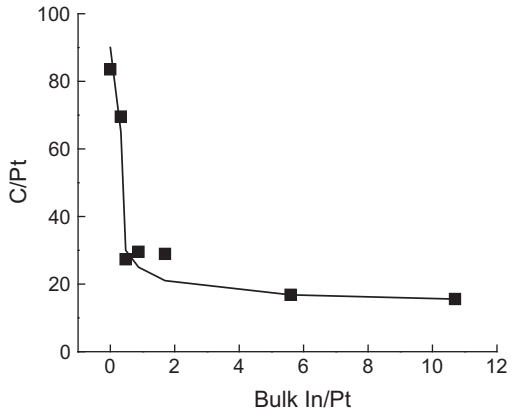

Fig. 14. Dependence of C/Pt ratio on bulk In/Pt ratio after 2 h time on stream of propane dehydrogenation. Reaction conditions: *T*: 873 K, m = 25 mg, C_2H_6: 20%, total flow rate: 60 cm^3/min, H_2/C_3H_8 = 1.25).

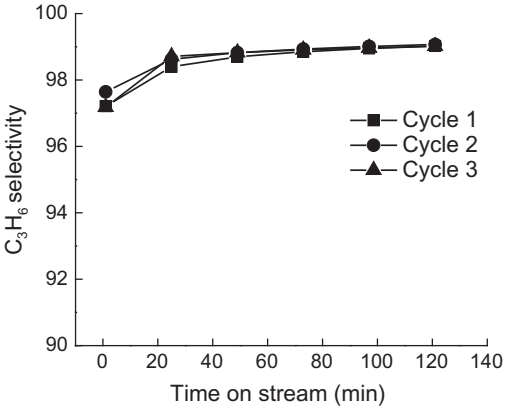

Fig. 16. Effects of catalyst cycling on selectivity of propene formation versus time on stream. Reaction conditions: *T*: 873 K, *m* = 25 mg, C_3H_8: 20%, total flow rate: 60 cm^3/min, H_2/C_2H_6 = 1.25).

respectively, of highly disordered graphite particles [52]. In single crystal graphite, the G band appears at 1575 cm^{-1} but shifts to higher frequencies with decreasing crystal size. For finite crystallites of graphite, the D band appears at 1355 cm^{-1} and is attributed to zone-boundary phonon vibrations. The ratio of the band intensities I_D/I_G has been used to estimate the size of graphite domains. For the spectra shown in Figs. 17 and 18, I_D/I_G = 1.3–1.5, from which it is deduced that the graphite domains are about 30 nm.

The extent to which graphitic deposits produced during alkane dehydrogenation are responsible for loss of catalyst activity with time on stream needs to be examined. Comparison of Figs. 10 and 14 shows that the amount of carbon deposited on Pt/Mg(In)(Al)O 0.48 after 2 h of time on stream is roughly the same during ethane and propane deposition, C/Pt ≈ 25. At the same time, Figs. 11 and 15 show that while the loss in ethane dehydrogenation activity is only 0.1%, the loss in activity under identical reaction conditions is 20% in the case of propane dehydrogenation. This difference in the extent of activity loss cannot be ascribed to the structure of the carbon, since, as discussed earlier, both ethane and propane produce carbonaceous deposits that are very similar in structure and size. A higher loss in activity during propane versus ethane dehydrogenation was also seen for Pt/Mg(Ga)(Al)O [32], but in that case, the amount of carbon deposited was more than twofold greater for ethane dehydrogenation. These observations were attributed to the greater ease with which precursors to the carbonaceous deposit produced from ethane rather than propane could migrate from the metallic particles where they are formed onto the support. Consistent with this interpretation, it was observed that following alkane dehydrogenation of propane, a greater loss in CO chemisorption capacity was observed than following ethane dehydrogenation. Given the strong similarities in the performance of Pt/Mg(In)(Al)O and Pt/Mg(Ga)(Al)O, we suggest that the precursors to carbon deposition produced during ethane dehydrogenation occurring on Pt/Mg(In)(Al)O transfer more readily to the support than do the carbon precursors produced during propane dehydrogenation. A discussion of the mechanism by which carbon deposition occurs on Pt/Mg(Al)O catalysts has been presented in Ref. [54]. The authors of this study note that surface science studies indicate that C—C bond cleavage of alkylidyne species formed on the surface of Pt leads to the formation of surface carbon atoms which then organize to form coke. It is also noted that propylidyne species are more stable to hydrogenation than ethylidyne species and, hence, more likely to lead to coke deposition.

A comparison of the performance of Pt/Mg(In)(Al)O 0.48 with that of Pt/Mg(Al)O, PtSn/Mg(Al)O 0.6, and Pt/Mg(Ga)(Al)O 2.9 is presented in Table 6. In each case, the catalyst exhibiting the highest activity was chosen. The M/Pt ratio given in this table is the stoichiometric ratio of the promoting element to the total amount of Pt in the catalyst. For Pt/Mg(Ga)(Al)O and Pt/Mg(In)(Al)O, the promoting element, Ga or In, is added during the synthesis of the support, whereas for PtSn/Mg(Al)O, the promoting element, Sn, is added by grafting Sn onto the Pt particles of Pt/Mg(Al)O [53]. For

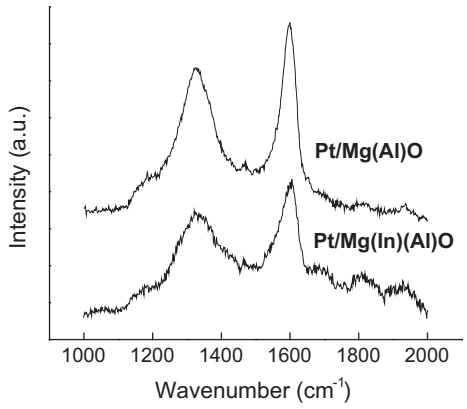

Fig. 17. Raman spectra of Pt/Mg(Al)O and Pt/Mg(In)(Al)O 0.88 after 2 h of time on stream for ethane dehydrogenation. Reaction conditions: *T*: 873 K, *m* = 25 mg, C_3H_8: 20%, total flow rate: 60 cm^3/min, H_2/C_2H_6 = 1.25).

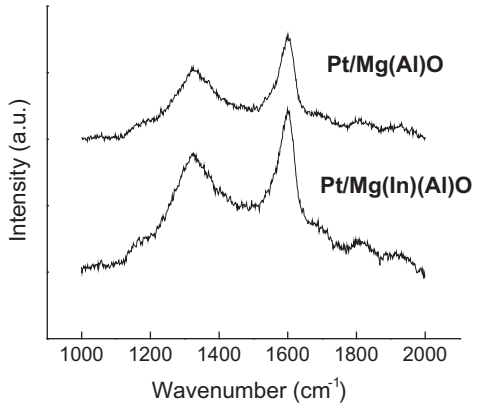

Fig. 18. Raman spectra of Pt/Mg(Al)O and Pt/Mg(In)(Al)O 0.88 catalysts after 2 h of time on stream for propane dehydrogenation.

ethane dehydrogenation, Pt/Mg(In)(Al)O 0.48, Pt/Mg(Ga)(Al)O 2.9, and PtSn/Mg(Al)O 0.6 exhibit comparable activities and selectivities. The rate of ethane dehydrogenation for these three catalysts is only slightly higher than that for Pt/Mg(Al)O, but the ethene selectivity for these three catalysts is ~37% higher than that for Pt/Mg(Al)O. The amount of carbon accumulated after 2 h of time on stream for Pt/Mg(In)(Al)O 0.48 and Pt/Mg(Ga)(Al)O 2.9 are comparable and significantly less than that for PtSn/Mg(Al)O and Pt/Mg(Al)O. The most notable difference among the catalysts is their stability with time on stream. The loss in activity during 2 h of time on stream for Pt/Mg(In)(Al)O 0.48 is an order of magnitude lower than that of Pt/Mg(Ga)(Al)O 2.9, PtSn/Mg(Al)O, and Pt/Mg(Al)O. Thus, Pt/Mg(In)(Al)O 0.48 gives the best performance for ethane dehydrogenation based on activity, ethene selectivity, accumulation of carbon, and particularly catalyst stability.

Table 6 shows that for propane dehydrogenation, the catalyst activity decreases in the order Pt/Mg(In)(Al)O 0.48 > Pt/Mg(Ga)(Al)O 2.9 > PtSn/Mg(Al)O 0.6 > PtGa/Mg(Al)O 3.0 > Pt/Mg(Al)O. However, the selectivity to propene is >98% for all of these catalysts except Pt/Mg(Al)O, for which the selectivity is 88%. The loss of activity with time on stream increases in the order Pt/Mg(In)(Al)O 0.48 < Pt/Mg(Ga)(Al)O 2.9 < PtSn/Mg(Al)O 0.6 < Pt/Mg(Al)O < PtGa/Mg(Al)O 3.0, and the accumulation of carbon decreases in the order Pt/Mg(Ga)(Al)O 2.9 < PtGa/Mg(Al)O 3.0 ≈ Pt/Mg(In)(Al)O 0.48 < PtSn/Mg(Al)O 0.6 < Pt/Mg(Al)O. Thus, Pt/Mg(In)(Al)O 0.48 gives the best performance for propane dehydrogenation based on activity, propene selectivity, and particularly catalyst stability, but not carbon accumulation.

It is evident from the preceding discussion that the performance of Pt/Mg(In)(Al)O 0.48 and Pt/Mg(Ga)(Al)O 2.9 is very similar in many respects and significantly superior to that of Pt/Mg(Al)O. As shown here, and previously for Pt/Mg(Ga)(Al)O 2.9 [17], H_2 reduction at 873 K results in the formation of PtIn and PtGa alloys, respectively. The formation of such alloys increases the selectivity of Pt for the alkane dehydrogenation and minimizes the formation of lower molecular products, such as methane and ethane, and also reduces the level of carbon deposition. The effects of alloy formation have also been reported for PtSn/Mg(Al)O and Sn-promoted Pt supported on other metal oxides [6,11,20,21,54].

The results of the present investigation demonstrate the optimal performance is achieved when the bulk In/Pt ratio is 0.48, for which case, analysis of EXAFS data indicates that the PtIn alloy formed contains only 12% In. This suggests that it is not necessary to form a stoichiometric alloy phase such as Pt_3In, which contains 25% In, in order to have a strong effect on catalytic properties of Pt. The electronic effect of In on Pt is evidenced by XAFS. As seen in Fig. 6, the incorporation of In into Pt nanoparticles results in an upward shift of Pt Fermi energy and, hence, a decrease in the d band vacancy. A similar shift has been also seen for PtSn alloys [55]. Both experimental and theoretical studies have shown that PtSn adsorbs ethene more weakly than pure Pt, and isotopic labeling studies conducted on PtSn/Mg(Al)O have shown that readsorption of ethene formed during ethane dehydrogenation is the primary cause of methane formation and the deposition of carbon [53,56]. Thus, it is reasonable to propose that In addition, similar with Sn addition, causes a decrease in alkene adsorption on Pt, leading to rapid desorption of alkenes and therefore high selectivity toward alkene production. Recent theoretical results for Pt_3Sn and Pt_3In alloys support this hypothesis [43].

4. Conclusion

Catalysts for the dehydrogenation of light alkanes have been prepared by dispersing Pt nanoparticles onto a calcined hydrotalcite-like support containing In and Al, Mg(In)(Al)O. Upon reduction at temperatures above 723 K, part of the In^{3+} cations present near the support surface and proximate to Pt are reduced and the resulting In atoms form a PtIn bimetallic alloy with the supported Pt nanoparticles. The average size of the Pt and PtIn particles is about 1 nm independent of the bulk In/Pt ratio of the catalyst. With increasing bulk In/Pt ratios, the fraction of the alloy consisting of

Table 6
Comparison of catalyst properties.

Catalyst	M/Pt	Activity, μmol/s/gcat		Selectivity, %		Deactivation, %		C/Pt, at/at	
		C2	C3	C2	C3	C2	C3	C2	C3
Pt/Mg(Al)O	0	22	18	62	88	5	44	110	73
Pt/Mg(In)(Al)O	0.48	29	67	98	98	0.1	20	23	27
Pt/Mg(Ga)(Al)O	2.9	28	53	100	99	1	29	27	11
PtSn/Mg(Al)O	0.6	27	47	98	99	2	39	54	38
PtGa/Mg(Al)O	3	18	26	97	98	22	55	48	25

In increases linearly and the fraction of Pt atoms at the alloy surface capable of adsorbing H_2 decreases. Evidence is also found for increasing In to Pt charge transfer with increasing bulk In/Pt ratio.

The activities of Pt/Mg(In)(Al) catalysts for ethane and propane dehydrogenation reactions are strong functions of the bulk In/Pt ratio. For both reactions, the maximum activity is achieved for a bulk In/Pt ratio of 0.48, corresponding to a PtIn alloy containing 12% In. The selectivities to ethene and propene are nearly 100% for Pt/Mg(In)(Al) 0.48. The alloying of In with Pt causes a significant decrease in the accumulation of C during both ethane and propane dehydrogenation. The accumulation of carbon decreases most significantly as the bulk In/Pt ratio increases from 0 to 0.48, and more slowly for higher In/Pt ratios. Whereas only 0.1% of the initial activity for ethane dehydrogenation is lost in 2 h on stream, 20% of the initial activity for propane dehydrogenation is lost over the same period. Since the size of the PtIn nanoparticles is unaffected by catalyst use, catalyst deactivation is attributed to the accumulation of carbon. While small domains (~30 nm) of graphitic carbon are formed during ethane and propane dehydrogenation, the location of their accumulation depends on the composition of the alkane undergoing dehydrogenation. During ethane dehydrogenation, carbon is accumulated primarily on the support, whereas during propane dehydrogenation, a part of the carbon also accumulates on the PtIn nanoparticles.

Acknowledgments

This work was supported by Chevron Energy and Technology Company. A portion of this research was conducted at the SHaRE User Facility, which is sponsored by the Division of Scientific User Facilities, Office of Basic Energy Sciences, US Department of Energy.

Appendix A. Supplementary material

Supplementary data associated with this article can be found, in the online version, at doi:10.1016/j.jcat.2011.06.008.

References

[1] P. Sun, G. Siddiqi, M. Chi, A.T. Bell, J. Catal. 274 (2010) 192–199.
[2] L.C. Loc, N.A. Gaidai, S.L. Kiperman, H.S. Thoang, N.M. Podklenova, S.B. Kogan, Kinetika i Kataliz 32 (1991).
[3] N.A. Pakhomov, Kinet. Catal. 42 (2001) 334–343.
[4] N. Homs, J. Llorca, M. Riera, J. Jolis, J.-L.G. Fierro, J. Sales, P.R. de la Piscina, J. Mol. Catal. A: Chem. 200 (2003) 251–259.
[5] E.L. Jablonski, A.A. Castro, O.A. Scelza, S.R. de Miguel, Appl. Catal. A: Gen. 183 (1999) 189–198.
[6] O.A. Barias, A. Holmen, E.A. Blekkan, in: B. Delmon, G.F. Froment (Eds.), Catalyst Deactivation, Elsevier Science Publ BV, Amsterdam, 1994, pp. 519–524.
[7] A.A. Castro, Catal. Lett. 22 (1993) 123–133.
[8] S. de Miguel, A. Castro, O. Scelza, J.L.G. Fierro, J. Soria, Catal. Lett. 36 (1996) 201–206.
[9] M. Larsson, B. Andersson, O.A. Barias, A. Holmen, in: B. Delmon, G.F. Froment (Eds.), Catalyst Deactivation, Elsevier Science Publ BV, Amsterdam, 1994, pp. 233–240.
[10] R.D. Cortright, J.M. Hill, J.A. Dumesic, Catal. Today 55 (2000) 213–223.
[11] A. Virnovskaia, E. Rytter, U. Olsbye, Ind. Eng. Chem. Res. 47 (2008) 7167–7177.
[12] A.D. Ballarini, C.G. Ricci, M.S.R. de, O.A. Scelza, Catal. Today 133–135 (2008) 28–34.
[13] L. Bednarova, C.E. Lyman, E. Rytter, A. Holmen, J. Catal. 211 (2002) 335–346.
[14] J. Salmones, J.-A. Wang, J.A. Galicia, G. Aguilar-Rios, J. Mol. Catal. A: Chem. 184 (2002) 203–213.
[15] H. Armendariz, A. Guzman, J.A. Toledo, M.E. Llanos, A. Vazquez, G. Aguilar-Rios, Appl. Catal. A 211 (2001) 69–80.
[16] J. Llorca, N. Homs, J. Leon, J. Sales, J.L.G. Fierro, d.l.P.P. Ramirez, Appl. Catal. A 189 (1999) 77–86.
[17] A.D. Ballarini, S.A. Bocanegra, A.A. Castro, M.S.R. de, O.A. Scelza, Catal. Lett. 129 (2009) 293–302.
[18] S.A. Bocanegra, A. Guerrero-Ruiz, M.S.R. de, O.A. Scelza, Appl. Catal. A 277 (2004) 11–22.
[19] C.L. Padro, M.S.R. De, A.A. Castro, O.A. Scelza, Stud. Surf. Sci. Catal. 111 (1997) 191–198.
[20] A. Virnovskaia, S. Jørgensen, J. Hafizovic, Ø. Prytz, E. Kleimenov, M. Hävecker, H. Bluhm, A. Knop-Gericke, R. Schlögl, U. Olsbye, Surf. Sci. 601 (2007) 30–43.
[21] A. Virnovskaia, S. Morandi, E. Rytter, G. Ghiotti, U. Olsbye, J. Phys. Chem. C 111 (2007) 14732–14742.
[22] J.H. Kwak, J. Hu, D. Mei, C.-W. Yi, D.H. Kim, C.H.F. Peden, L.F. Allard, J. Szanyi, Science 325 (2009) 1670–1673.
[23] H.H.C.M. Pinxt, B.F.M. Kuster, D.C. Koningsberger, G.B. Marin, Catal. Today 39 (1998) 351–361.
[24] J.M. Ramallo-Lopez, G.F. Santori, L. Giovanetti, M.L. Casella, O.A. Ferretti, F.G. Requejo, J. Phys. Chem. B 107 (2003) 11441–11451.
[25] G.J. Siri, J.M. Ramallo-Lopez, M.L. Casella, J.L.G. Fierro, F.G. Requejo, O.A. Ferretti, Appl. Catal. A 278 (2005) 239–249.
[26] E. Antolini, F. Colmati, E.R. Gonzalez, J. Power Sources 193 (2009) 555–561.
[27] V. Radmilovic, T.J. Richardson, S.J. Chen, P.N. Ross Jr, J. Catal. 232 (2005) 199–209.
[28] N. Nava, P. Del Angel, J. Salmones, E. Baggio-Saitovitch, P. Santiago, Appl. Surf. Sci. 253 (2007) 9215–9220.
[29] C. Vértes, E. Tálas, I. Czakó-Nagy, J. Ryczkowski, S. Göbölös, A. Vértes, J. Margitfalvi, Appl. Catal. 68 (1991) 149–159.
[30] M.C. Roman-Martinez, J.A. Macia-Agullo, I.M.J. Vilella, D. Cazorla-Amoros, H. Yamashita, J. Phys. Chem. C 111 (2007) 4710–4716.
[31] F.B. Passos, D.A.G. Aranda, M. Schmal, J. Catal. 178 (1998) 478–488.
[32] G. Siddiqi, P. Sun, V. Galvita, A.T. Bell, J. Catal. 274 (2010) 200–206.
[33] (a) M. Neville, J. Synchrotron Radiat. 8 (2001) 96–100;
(b) B. Ravel, M. Neville, J. Synchrotron Radiat. 12 (2005) 537–541.
[34] P. Villars, L.D. Calvert, W.B. Pearson, Pearson's Handbook of Crystallographic Data for Intermetallic Phases, ASM International, Materials Park, Ohio, 1991.
[35] P.B. Weisz, C.D. Prater, in: W.G. Frankenburg, V.I. Komarewsky, E.K. Rideal (Eds), Advances in Catalysis, vol. 6, Academic Press, New York, 1954, pp. 143–196.
[36] M. Bellotto, B. Rebours, O. Clause, J. Lynch, D. Bazin, E. Elkaim, J. Phys. Chem. 100 (1996) 8527–8534.
[37] E. Bus, B.J.A. van, Phys. Chem. Chem. Phys. 9 (2007) 2894–2902.
[38] J. Fearon, G.W. Watson, J. Mater. Chem. 16 (2006) 1989–1996.
[39] S. Abelló, J. Pérez-Ramírez, Micropor. Mesopor. Mater. 96 (2006) 102–108.
[40] T. Bielz, H. Lorenz, W. Jochum, R. Kaindl, F. Klauser, B. Klötzer, S. Penner, J. Phys. Chem. C 114 (2010) 9022–9029.
[41] H.-L. Xin, N. Schweitzer, E. Nikolla, S. Linic, J. Chem. Phys. 132 (2010). pp. 111101/111101–111101/111104.
[42] X. Chen, W. Chu, Q. Cai, D. Xia, Z. Wu, Z. Wu, Radiat. Phys. Chem. 75 (2006) 1622–1625.
[43] E. Bus, B.J.A. Van, J. Phys. Chem. C 111 (2007) 9761–9768.
[44] J.T. Miller, A.J. Kropf, Y. Zha, J.R. Regalbuto, L. Delannoy, C. Louis, E. Bus, J.A. van Bokhoven, J. Catal. 240 (2006) 222–234.
[45] A. Yevick, A.I. Frenkel, Phys. Rev. B: Condens. Matter Mater. Phys. 81 (2010). pp. 115451/115451–115451/115457.
[46] A.N. Mansour, J.W. Cook Jr., D.E. Sayers, J. Phys. Chem. 88 (1984) 2330–2334.
[47] Y.-S. Lee, K.-Y. Lim, Y.-D. Chung, C.-N. Whang, Y. Jeon, Surf. Interface Anal. 30 (2000) 475–478.
[48] A.L. Ankudinov, J.J. Rehr, J.J. Low, S.R. Bare, J. Synchrotron Radiat. 8 (2001) 578–580.
[49] D. Bazin, D. Sayers, J.J. Rehr, C. Mottet, J. Phys. Chem. B 101 (1997) 5332–5336.
[50] M.W. Tew, J.T. Miller, B.J.A. van Bokhoven, J. Phys. Chem. C 113 (2009) 15140–15147.
[51] J.H. Kim, S.M. Choi, S.H. Nam, M.H. Seo, S.H. Choi, W.B. Kim, Appl. Catal. B 82 (2008) 89–102.
[52] F. Tuinstra, J.L. Koenig, J. Chem. Phys. 53 (1970) 1126–1130.
[53] V. Galvita, G. Siddiqi, P. Sun, A.T. Bell, J. Catal. 271 (2010) 209–219.
[54] Y. Zhang, Y. Zhou, A. Qiu, Y. Wang, Y. Xu, P. Wu, Catal. Commun. 7 (2006) 860–866.
[55] N. Schweitzer, H. Xin, E. Nikolla, J. Miller, S. Linic, Topics Catal. 53 (2010) 348–356.
[56] R.M. Watwe, R.D. Cortright, M. Mavrikakis, J.K. Norskov, J.A. Dumesic, J. Chem. Phys. 114 (2001) 4663–4668.